The Astrophysical Journal, 885:155 (11pp), 2019 November 10 https://doi.org/10.3847/1538-4357/ab3eb9

Spatially Resolved Stellar Kinematics of the Ultra-diffuse Galaxy Dragonfly 44. II. Constraints on Fuzzy Dark Matter

Asher Wasserman[1], Pieter van Dokkum[2], Aaron J. Romanowsky[3,4], Jean Brodie[1,4], Shany Danieli[2], Duncan A. Forbes[5], Roberto Abraham[6], Christopher Martin[7], Matt Matuszewski[7], Alexa Villaume[1], John Tamanas[8,9], and Stefano Profumo[8,9]
[1] Department of Astronomy & Astrophysics, University of California Santa Cruz, Santa Cruz, CA 95064, USA; adwasser@ucsc.edu
[2] Astronomy Department, Yale University, New Haven, CT 06511, USA
[3] Department of Physics & Astronomy, San José State University, One Washington Square, San Jose, CA 95192, USA
[4] University of California Observatories, 1156 High Street, Santa Cruz, CA 95064, USA
[5] Centre for Astrophysics and Supercomputing, Swinburne University, Hawthorn, VIC 3122, Australia
[6] Department of Astronomy & Astrophysics, University of Toronto, 50 St. George Street, Toronto, ON M5S 3H4, Canada
[7] Cahill Center for Astrophysics, California Institute of Technology, 1216 East California Boulevard, Mail code 278-17, Pasadena, CA 91125, USA
[8] Department of Physics, 1156 High St., University of California Santa Cruz, Santa Cruz, CA 95064, USA
[9] Santa Cruz Institute for Particle Physics, 1156 High Street, Santa Cruz, CA 95064, USA
Received 2019 May 23; revised 2019 August 26; accepted 2019 August 26; published 2019 November 11

Abstract

Given the absence of directly detected dark matter (DM) as weakly interacting massive particles, there is strong interest in the possibility that DM is an ultralight scalar field, here denoted as "fuzzy" DM. Ultra-diffuse galaxies, with the sizes of giant galaxies and the luminosities of dwarf galaxies, have a wide range of DM halo masses, thus providing new opportunities for exploring the connections between galaxies and their DM halos. Following up on new integral field unit spectroscopic observations and dynamics modeling of the DM-dominated ultra-diffuse galaxy Dragonfly 44 in the outskirts of the Coma Cluster, we present models of fuzzy DM constrained by the stellar dynamics of this galaxy. We infer a scalar field mass of $\sim 3 \times 10^{-22}$ eV, consistent with other constraints from galaxy dynamics but in tension with constraints from Lyα forest power spectrum modeling. While we are unable to statistically distinguish between fuzzy DM and "normal" cold DM models, we find that the inferred properties of the fuzzy DM halo satisfy a number of predictions for halos in a fuzzy DM cosmology. In particular, we find good agreement with the predicted core size–halo mass relation and the predicted transition radius between the quantum pressure-dominated inner region and the outer halo region.

Key words: dark matter – galaxies: halos – galaxies: individual (Dragonfly 44) – galaxies: kinematics and dynamics

1. Introduction

The concordant cosmological model of dark energy plus cold dark matter (ΛCDM) has had remarkable successes in describing the large-scale structure of the universe (e.g., Tegmark et al. 2006; Planck Collaboration et al. 2018). However, there have been a number of small-scale challenges to this picture concerning the inner density structure of dark matter (DM) halos and the relative numbers of subhalos (e.g., Weinberg et al. 2015; Bullock & Boylan-Kolchin 2017, and references therein). Many authors have proposed solutions to these problems that involve a more detailed treatment of the baryonic physics of galaxy formation (e.g., Pontzen & Governato 2012; Martizzi et al. 2013; Schaller et al. 2015). Furthermore, given the continued absence of directly detected DM particles (Marrodán Undagoitia & Rauch 2016; Akerib et al. 2017; Aprile et al. 2018), attempts to explain these astrophysical discrepancies with modifications of the physics of DM have become increasingly appealing. Frequently considered modifications include allowing for self-interactions (e.g., Carlson et al. 1992; Rocha et al. 2013; Wittman et al. 2018) and increasing the DM temperature at the time of thermal decoupling (Warm DM; e.g., Davis et al. 1981; Lovell et al. 2017; Bozek et al. 2019). For overviews of the intersection of astrophysics and particle physics searches for DM, we refer readers to the reviews of Bertone et al. (2005), Profumo (2017), and Buckley & Peter (2018).

One promising class of models posits that the DM particle is an extremely low-mass ($\ll 1$ eV)[10] spin-0 boson (i.e., a scalar field) manifesting quantum mechanical wave-like behavior on astrophysical scales (∼kiloparsec; Colpi et al. 1986; Lee & Koh 1996; Hu et al. 2000; Matos et al. 2009; Hui et al. 2017). Axions, a proposed solution to the strong charge-parity problem in particle physics (Peccei & Quinn 1977; Dine et al. 1981), are a well-motivated class of models that provide one such candidate DM particle. There are a variety of names for these DM models: ultralight axion DM, scalar field DM, Bose–Einstein condensate DM, wave DM, or fuzzy DM. Here we adopt the term Fuzzy Dark Matter (FDM) for ultralight ($m \sim 10^{-22}$ eV) nonthermal (i.e., restricted to the ground state) models lacking self-interaction. We refer to the mass of the DM scalar field in this model in its dimensionless form as $m_{22} = m/10^{-22}$ eV.

We note that for any model in which an ultralight scalar field is the dominant contributor to DM, its production mechanism must necessarily be nonthermal (Marsh 2016), in contrast with the thermal production of weakly interacting massive particles in the standard CDM cosmology (Bringmann & Hofmann 2007). Thermal production of such a low mass of DM would lead to hot (i.e., ultrarelativistic) DM, in conflict with observations of the matter power spectrum and the cosmic

[10] For particle masses, we use the convention that $c = 1$, giving mass and energy the same physical dimensions.

microwave background (CMB; e.g., Viel et al. 2005). For a broad overview of FDM cosmologies, we refer interested readers to Marsh (2016) and Hui et al. (2017).

The salient phenomena associated with FDM cosmologies are a cutoff in the halo mass function below $\sim 10^9\,M_\odot$, and distinct density cores in the inner $\sim$1 kpc of DM halos, with a lighter scalar field mass resulting in a higher halo mass cutoff and a more massive inner core (Hu et al. 2000). This cutoff in the halo mass distribution implies less correlation of structure on smaller scales and the delayed formation of galaxies relative to CDM. The measured CMB and galaxy power spectra imply that, if FDM makes up the majority of DM in the universe, m_{22} must be $\gtrsim 10^{-3}$ (Hlozek et al. 2015). Constraints from the Lyα forest power spectrum imply that $m_{22} \gtrsim 1$, with some models excluding scalar field masses up to $m_{22} \sim 30$ (Armengaud et al. 2017; Nori et al. 2019). Complementary constraints on FDM models from both high redshift galaxy luminosity functions and the Milky Way satellite luminosity function are also consistent with $m_{22} \gtrsim 1$ (Bozek et al. 2015; Schive et al. 2016; Nadler et al. 2019).

The stellar dynamics of nearby galaxies offer further opportunities to test FDM models. The inner density structures of DM halos that form in an FDM cosmology follow a stationary wave, or soliton, solution to the Schrödinger–Poisson equation (Schive et al. 2014a; Marsh & Pop 2015). In the outer region the halo density profile transitions to a normal CDM halo profile (e.g., a Navarro–Frenk–White (NFW) profile; Navarro et al. 1997). The sizes of these cores are predicted to scale inversely with halo mass, while the symmetry of the soliton solution requires the core density to scale inversely with the core size (Schive et al. 2014a). Higher mass halos are therefore predicted to have smaller but denser cores.

Many previous studies of FDM density profiles in galaxies have focused on either dwarf spheroidal (dSph) or ultrafaint dwarf (UFD) galaxies (e.g., Lora & Magaña 2014; Marsh & Pop 2015; Chen et al. 2017; González-Morales et al. 2017), as their high dynamical mass-to-light ratios minimize the impact of systematic assumptions about the stellar mass distribution. Studies have generally found $m_{22} \sim 1$ (within a factor of a few), in slight tension with the Lyα constraints. Calabrese & Spergel (2016) found that the stellar kinematics of two UFDs were consistent with $m_{22} \sim 4$, though they noted the lack of kinematic measurements outside of the inferred core radius. More recently, Marsh & Niemeyer (2019) applied the stochastic density fluctuation model of El-Zant et al. (2016) to study how FDM would cause dynamical heating of the star cluster in the UFD Eridanus II. They argued that the survival of the EriII star cluster implies $m_{22} \gtrsim 1000$, whereas the existence of EriII itself implies $m_{22} \gtrsim 10$.

Looking toward more massive galaxies to probe FDM scaling relations presents increasing difficulties in disentangling the baryonic and dark mass components. In the halo mass range of 10^{10}–$10^{11}\,M_\odot$, low surface brightness (LSB) galaxies have proven to be the most amenable to analysis. Bernal et al. (2018) modeled the rotation curves of 18 LSBs, and their results favored a lower value of $m_{22} \sim 0.05$ (though see Bar et al. (2019) for a discussion of the impact of the baryons on the FDM density structure). Bar et al. (2018) also modeled the rotation curves of LSBs under the assumption of the previously mentioned soliton–halo scaling relations, finding that the data were in tension with $1 \lesssim m_{22} \lesssim 10$.

With the discovery of a vast population of even lower surface brightness "ultra-diffuse" galaxies (UDGs; Koda et al. 2015; Mihos et al. 2015; van Dokkum et al. 2015), we now have more opportunities to test FDM in a broader range of galaxy masses and environments. The Coma Cluster UDG Dragonfly 44 was shown to have a large stellar velocity dispersion, corresponding to a DM halo with a mass on the order of that of the Milky Way (van Dokkum et al. 2016). In a companion paper, van Dokkum et al. (2019; hereafter Paper I), we present new spatially resolved spectroscopy of Dragonfly 44, confirming that the potential of the galaxy is indeed dominated by DM. In this work, we address the question of whether or not the dynamics of Dragonfly 44 are consistent with FDM.

Throughout this work we assume the Planck Collaboration et al. (2018) values of relevant cosmological parameters, including $H_0 = 67.66\,\mathrm{km\ s^{-1}\ Mpc^{-1}}$ and $\Omega_m = 0.3111$.

In Section 2 we summarize the photometric and spectroscopic data for Dragonfly 44. We describe the Jeans modeling formalism and mass modeling assumptions in Section 3. In Section 4 we present our derived constraints on FDM models, and we place our results in context with other FDM studies in Section 5.

2. Data

Readers interested in a detailed description of the spectroscopic observations, data reduction, and kinematic extraction are referred to Paper I; here we provide a brief summary of the observational data for Dragonfly 44. We adopt a standard distance to Coma of 100 Mpc for the galaxy, which has an associated distance modulus $m - M = 35$ and an angular distance conversion factor of 0.485 kpc arcsec^{-1}.

Using the V_{606} *Hubble Space Telescope* (*HST*) WFC3/UVIS imaging data presented by van Dokkum et al. (2017), we modeled the stellar light of Dragonfly 44 with a Sérsic surface brightness profile, deriving a total luminosity of $L_V = 2.33 \times 10^8\,L_{\odot,V}$, a major-axis effective radius of $R_e = 4.7$ kpc, a Sérsic index of $n = 0.94$, and an axis ratio of $b/a = 0.68$. For our modeling purposes, we adopt the circularized effective radius of $R_{e,\mathrm{circ}} = R_e\sqrt{b/a} = 3.87$ kpc.

We obtained integral field unit spectroscopy of Dragonfly 44 with the Keck Cosmic Web Imager in the first half of 2018, with 17 hr of exposure time on target and an additional 8 hr on sky. We used the medium slicer with the BM grating, yielding a field of view of $16'' \times 20''$ and a spectral resolution of $R \sim 4000$.

For reducing the data to rectified, wavelength calibrated cubes, we used the public Keck-maintained pipeline, KDERP.[11] We aligned the individual science exposures by fitting a 2D model of the flux from the *HST* imaging data and interpolating to a common spatial grid with a spatial resolution of $\sim 1\farcs2$. We subtracted the sky spectrum using a principle component analysis technique—see Paper I for further details. The final signal-to-noise ratio in the optimally combined spectrum was 48 per pixel or 96 Å^{-1}.

We extracted spectra in nine elliptical apertures following the isophotes of the galaxy. We modeled the stellar kinematic line-of-sight velocity distribution (LOSVD) as a fourth-order Gauss–Hermite function, and we fitted the LOSVD in each of these apertures by convolving it with both a high-resolution

[11] https://github.com/Keck-DataReductionPipelines/KcwiDRP

template spectrum of a synthetic stellar population and the instrumental line profile (including a wavelength-dependent resolution). From varying the ages and metallicities of the chosen stellar population template, we found the most likely values for an age of 10 Gyr and a metallicity of $[\mathrm{Fe/H}] = -1.25$. For each spectrum we found the best fitting central velocity and higher order (second, third, and fourth) moments of the LOSVD using a Markov Chain Monte Carlo (MCMC) simulation.

The radius of a given aperture is defined as the flux-weighted average pixel radius. There is little evidence for rotational motion in Dragonfly 44, with $v/\sigma \lesssim 0.25$ along the minor axis and $v/\sigma \lesssim 0.1$ along the major axis. We computed the effective rms velocity within each aperture as $v_{\mathrm{rms}}^2 = (v - v_{\mathrm{sys}})^2 + \sigma^2$.

3. Dynamical Modeling

We use the spherical Jeans modeling formalism presented in Wasserman et al. (2018), using an updated, publicly available modeling code.[12] Under the assumptions of dynamical equilibrium and spherical symmetry, the model predicts the LOS velocity dispersion as a function of projected galactocentric radius. See Hayashi & Obata (2019) for a discussion of the systematic uncertainty associated with applying spherical models to non-spherical systems. The main components of the model are the mass profile, $M(r)$, the tracer volume density profile, $\nu(r)$, and the orbital anisotropy profile of the tracers, $\beta_{\mathrm{ani}}(r)$. The orbital anisotropy for a spherically symmetric system is defined as

$$\beta_{\mathrm{ani}} = 1 - \sigma_t^2/\sigma_r^2, \tag{1}$$

where σ_t and σ_r are the tangential and radial components of the velocity dispersion.

We can compute the mean squared LOS velocity as

$$\sigma_{\mathrm{los}}^2(R) = \frac{2G}{I(R)} \int_R^\infty K_\beta(r, R)\nu(r)M(r)\frac{dr}{r}, \tag{2}$$

where $I(R)$ is the tracer surface density profile and $K_\beta(r, R)$ is the anisotropy projection kernel. For our adopted constant anisotropy profile, the functional form of this projection kernel is given by Mamon & Łokas (2005), Equation (A16).

We set the stellar tracer density distribution to follow the Sérsic distribution of the starlight. We assume that the stellar mass distribution follows the same Sérsic luminosity distribution used for the tracers, with the local stellar mass density given by the spatially invariant stellar mass-to-light ratio, Υ_*, multiplied by the stellar luminosity density.

3.1. Halo Models

For the DM halo, we construct a flexible double-power-law model with a soliton core. A generalized form of the NFW model (Navarro et al. 1997) is given by

$$\rho_{\alpha\beta\gamma}(r) = \rho_s \left(\frac{r}{r_s}\right)^{-\gamma} \left(1 + \left(\frac{r}{r_s}\right)^{\alpha}\right)^{(\gamma-\beta)/\alpha}, \tag{3}$$

where ρ_s is the scale density, r_s is the scale radius, γ is the negative inner log slope, β is the negative outer log slope, and α controls the sharpness of the transition between the two slopes (Hernquist 1990; Di Cintio et al. 2014). For $(\alpha, \beta, \gamma) = (1, 3, 1)$, this is the typical NFW profile, which we assume to be an appropriate approximation for CDM halos in the absence of baryonic effects or FDM cores.

The inner soliton core region from FDM has the density profile

$$\rho_{\mathrm{soliton}}(r) = \rho_{\mathrm{sol}} \left(1 + \left(\frac{r}{r_{\mathrm{sol}}}\right)^2\right)^{-8}, \tag{4}$$

where ρ_{sol} and r_{sol} are the soliton scale density and scale radius, respectively (Schive et al. 2014a; Marsh & Pop 2015; Robles et al. 2019). Note that we use a slightly different definition of the soliton radius than Schive et al. (2014a) and Robles et al. (2019); their core radius, r_c, refers to the radius where the density has fallen to half of the central density, and it is equivalent to 0.3017 r_{sol}. In addition to eliminating a numeric constant from the equations, our choice of definition for the soliton radius makes the ratio of the transition radius to the soliton radius near unity (see Section 5.3).

From the symmetry of the soliton solution, the soliton scale density and radius are related to the scalar field mass as

$$\frac{\rho_{\mathrm{sol}}}{M_\odot\,\mathrm{kpc}^{-3}} = 8.755 \times 10^6\, h^{-2}\, m_{22}^{-2} \left(\frac{r_{\mathrm{sol}}}{\mathrm{kpc}}\right)^{-4}, \tag{5}$$

where h is the Hubble parameter in units of 100 Mpc km s^{-1}, and m_{22} is the scalar field mass in units of 10^{-22} eV (Marsh & Pop 2015).

We match the inner soliton profile with the outer $\alpha\beta\gamma$ profile at the transition radius, r_t, by finding the root of the function corresponding to the difference between the two profiles. This guarantees that the density profile,

$$\rho(r) = \begin{cases} \rho_{\mathrm{soliton}}(r) & r < r_t \\ \rho_{\alpha\beta\gamma}(r) & r \geqslant r_t, \end{cases} \tag{6}$$

is a continuous function, and the transition radius is thus fixed for a given set of outer halo and soliton parameters. We reject any model that fails to converge due to the inner profile being less dense than the outer profile at all radii. The transition radius is found in simulations to be a factor of a few times the core radius of the soliton, and the transition between the soliton and normal CDM profiles is sharp (Schive et al. 2014a; Mocz et al. 2017). While FDM halo density profiles are continuous, their density derivatives are not.

The enclosed mass in the $\alpha\beta\gamma$ model is

$$M_{\alpha\beta\gamma}(r) = \frac{4\pi\rho_s r_s^3}{\omega} \left(\frac{r}{r_s}\right)^{\omega} {}_2F_1\left[\frac{\omega}{\alpha}, \frac{\beta-\gamma}{\alpha}, 1 + \frac{\omega}{\alpha}; -x^\alpha\right], \tag{7}$$

where $\omega = 3 - \gamma$ and ${}_2F_1$ is the hypergeometric function. For the limiting case of the NFW profile, this simplifies to

$$M_{\mathrm{NFW}}(r) = 4\pi\rho_s r_s^3 \left[\ln\left(1 + \frac{r}{r_s}\right) - \frac{r}{r_s + r}\right]. \tag{8}$$

[12] http://github.com/adwasser/Slomo.jl

Table 1
Coefficients for the Analytic Solution to the Soliton Enclosed Mass Profile (Equation (10))

k_0	k_1	k_2	k_3	k_4	k_5	k_6	k_7
27720	17325	−1155	−4235	−2625	−903	−175	−15

The enclosed mass of the soliton has an analytic form[13] and is given by

$$\begin{aligned} M_{\rm soliton}(r) &= \int_0^r 4\pi\tilde{r}^2\rho_{\rm soliton}(\tilde{r})d\tilde{r} \\ &= 4\pi\rho_{\rm sol}r_{\rm sol}^3\int_0^{r/r_{\rm sol}} x^2(1+x^2)^{-8}\,dx \\ &= 4\pi\rho_{\rm sol}r_{\rm sol}^3\int_0^{\theta} \tan^2(\theta)\sec^{-16}(\theta)\sec^2(\theta)\,d\theta \\ &= 4\pi\rho_{\rm sol}r_{\rm sol}^3\int_0^{\theta} \sin^2(\theta)\cos^{12}(\theta)\,d\theta, \end{aligned} \tag{9}$$

where in the second-to-last line we have used the trigonometric substitution $r/r_{\rm sol} = \tan(\theta)$. The integral in the last line can then be iteratively integrated by parts, yielding the following solution.

$$M_{\rm soliton}(r) = M_{\rm sol}\frac{1}{K}\left[k_0\theta + \sum_{i=1}^{7} k_i \sin(2i\theta)\right], \tag{10}$$

where $M_{\rm sol} = 4\pi\rho_{\rm sol}r_{\rm sol}^3$, $K = 1720{,}320$, and the other constant factors are given in Table 1 below.

From Equation (5), we can also express $M_{\rm sol}$ as

$$M_{\rm sol} = 1.1\times10^8\,M_\odot\,h^{-2}\,m_{22}^{-2}\left(\frac{r_{\rm sol}}{\rm kpc}\right)^{-1}. \tag{11}$$

Our generic halo mass profile is then given by

$$M(r) = \begin{cases} M_{\rm soliton}(r) & r < r_t \\ \Delta M_{\alpha\beta\gamma}(r) + M_{\rm soliton}(r_t) & r \geqslant r_t \end{cases}, \tag{12}$$

where $\Delta M_{\alpha\beta\gamma}(r) = M_{\alpha\beta\gamma}(r) - M_{\alpha\beta\gamma}(r_t)$.

We parameterize the halo with the virial mass and concentration, using the "200c" convention such that the virial radius is given by the relation

$$M(r_{\rm 200c}) = 200\rho_{\rm crit}\frac{4\pi}{3}r_{\rm 200c}^3 \tag{13}$$

and $c_{\rm 200c} = r_{\rm 200c}/r_{-2}$. Note that here we use the convention that the halo concentration is given by the radius where the halo log slope is equal to −2. This is related to the halo scale radius as

$$r_{-2} = \left(\frac{2-\gamma}{\beta-2}\right)^{1/\alpha} r_s. \tag{14}$$

Generally speaking, we must be careful in our definition of the halo virial mass and concentration. Since the soliton core contributes to the mass of a halo, the outer halo density and radius scale parameters for an FDM halo of a given virial mass and concentration are necessarily different than those for a normal CDM halo.

However, from the predicted scaling relation between soliton core mass and halo mass, we would expect a $10^{10}\,M_\odot$ halo to have $\lesssim$1% of its mass locked up in the soliton core, with this fraction decreasing with increasing halo mass (Robles et al. 2019). Thus, given the expected halo mass range of Dragonfly 44 of $\sim10^{11}$–$10^{12}\,M_\odot$, we assume that the differences in the outer halo scale parameters in the FDM and CDM models at fixed halo mass and concentration are negligible. We later verify the validity of this assumption by comparing the inferred virial mass with one computed from the posterior mass profile, finding a negligible difference.

This generic double-power-law plus soliton halo model has eight free parameters ($\beta_{\rm ani}$, $M_{\rm 200c}$, $c_{\rm 200c}$, α, β, γ, m_{22}, $r_{\rm sol}$) and it would be poorly constrained by the available kinematic data. Thus, we consider the following constraints.

We impose a prior on $c_{\rm 200c}$ by using the halo mass–concentration relation (HMCR) from Diemer & Kravtsov (2015). Practically, this is accomplished by sampling both $M_{\rm 200c}$ and $c_{\rm 200c}$, then using a log-normal prior on $c_{\rm 200c}$ whose mean is the HMCR prediction conditioned on the sampled $M_{\rm 200c}$, and whose scatter is 0.16 dex.

We consider two possibilities for the $\alpha\beta\gamma$ slope parameters. First, in the limit of no baryonic effects, we assume the outer halo follows an NFW profile with $(\alpha,\ \beta,\ \gamma) = (1,\ 3,\ 1)$. Alternatively assuming that baryonic feedback—such as cycles of bursty star formation—plays an important role, we use the halo scaling relations from the hydrodynamics simulations of Di Cintio et al. (2014), which map variation in $x = \log(M_*/M_{\rm vir})$ to α, β, and γ (see their Equation (3), also copied below as Equation (15)).

$$\begin{aligned} \alpha &= 2.94 - \log_{10}[(10^{x+2.33})^{-1.08} + (10^{x+2.33})^{2.29}] \\ \beta &= 4.23 + 1.34x + 0.26x^2 \\ \gamma &= -0.06 + \log_{10}[(10^{x+2.56})^{-0.68} + (10^{x+2.56})]. \end{aligned} \tag{15}$$

For Dragonfly 44, this results in a shallower CDM halo, with $\gamma \sim 0.3$.

To summarize, in addition to the CDM halo models described in Paper I, we have added two halo models by including the soliton core component from the FDM model, with both NFW and $\alpha\beta\gamma$ outer halo profiles.

Despite the constraints of the above assumptions, the task of inferring the properties of an FDM halo in Dragonfly 44 are substantial. Figure 1 illustrates the difficulty by comparing velocity dispersion profiles from expected FDM halo models with their CDM counterparts.

3.2. Bayesian Inference

We use a Gaussian likelihood to model the stellar velocity dispersion data, $\sigma_i \pm \delta\sigma_i$ in apertures with projected galactocentric radii, R_i. For a given halo model and model parameters, the predicted velocity dispersion, $\sigma_{\rm J}$, is modeled by Equation (2). The log likelihood is thus

$$\ln\mathcal{L} = \sum_i -\frac{1}{2}\left(\ln(2\pi\delta\sigma_i^2) + \left(\frac{\sigma_i - \sigma_{\rm J}(R_i)}{\delta\sigma_i}\right)^2\right). \tag{16}$$

We use uniform priors over the log of the halo mass, scalar field mass, and soliton scale radius. For the orbital anisotropy, we use a uniform prior over the symmetrized anisotropy parameter, $\tilde{\beta}_{\rm ani} = -\log_{10}(1-\beta_{\rm ani})$. This ensures that radial

[13] The existence of such an analytic form was noted by Marsh & Pop (2015), but the derivation of this profile was left as an exercise to the reader.

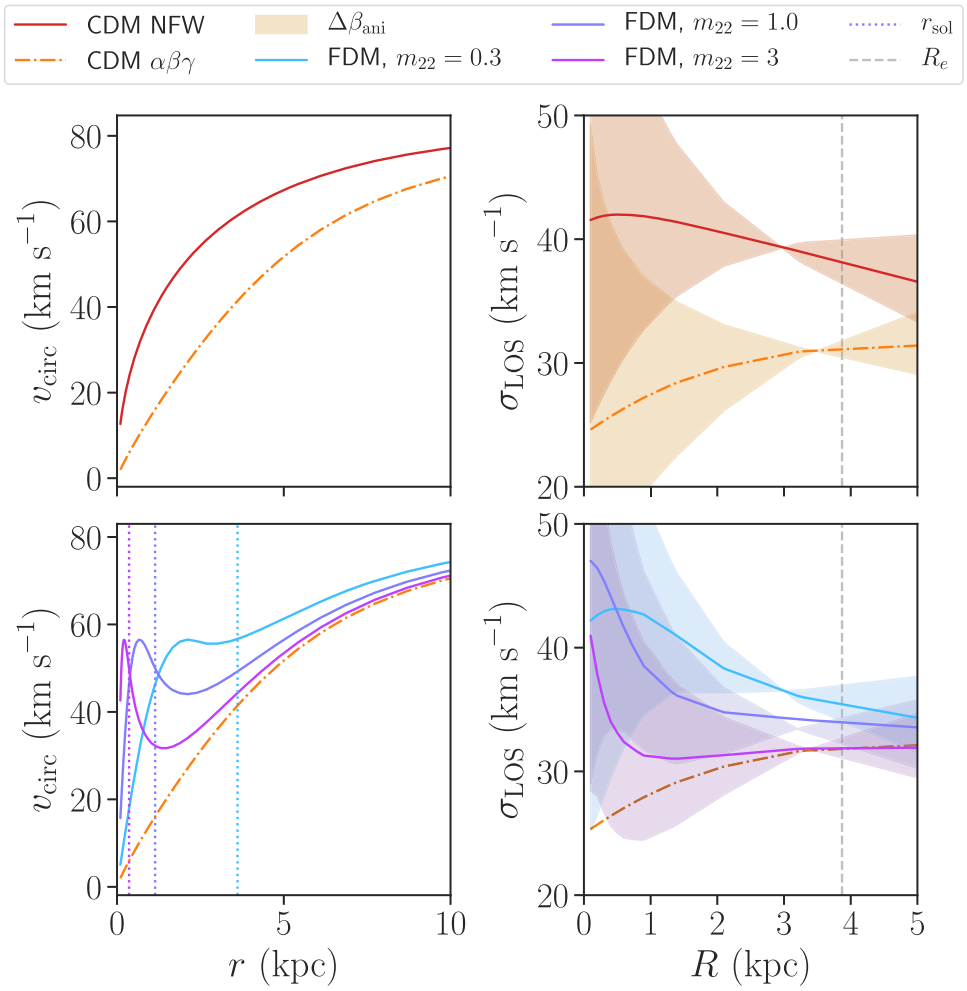

Figure 1. Illustration of mass models and their associated velocity dispersion profiles for different halo models described in Section 3.1. The top panels show CDM models with $\log_{10} M_{200c}/M_\odot = 11$, $c_{200c} = 10.5$, and $r_s = 9.3$ kpc. The red solid line shows a cuspy NFW halo and the orange dotted–dashed line shows a cored $\alpha\beta\gamma$ halo. The bottom panels show FDM halos with an outer $\alpha\beta\gamma$ halo profile (plotted again for comparison) for a range of possible values of m_{22}. The left-hand panels show the circular velocity profile associated to the halo, while the right-hand panels show the line-of-sight velocity dispersion profile. The range of orbital anisotropy values (from $\beta_{\rm ani} = -1$ to 0.5) is shown by the shaded region, with the line indicating the isotropic ($\beta_{\rm ani} = 0$) profile. Tangentially biased profiles ($\beta_{\rm ani} < 0$) generally display velocity dispersion profiles that increase with radius, while radially biased profiles generally fall with radius. In the bottom left panel, the dotted lines show the expected soliton scale radius associated to each FDM halo (see Section 5.2). As the FDM scalar field mass gets larger, the profile approaches its CDM analog, with the deviations occurring on increasingly smaller scales. FDM is more "detectable" for lower m_{22} values where there is more mass in the soliton core. However, the projection of this mass profile into an observable velocity dispersion tends to wash out this signal (demonstrating the mass–anisotropy degeneracy). Furthermore even with a known anisotropy parameter, the FDM signal is degenerate with the inner DM slope (i.e., cored or cuspy).

and tangential orbits are given equal weight. We use the HMCR as a prior for the concentration, as described in the previous section. For the stellar mass-to-light ratio, we use a log-normal distribution with mean $\log_{10} \Upsilon_{*,V} = \log_{10}(1.5)$ and a scatter of 0.1 dex. Here, the mean value chosen is typical of an old, low metallicity stellar population, while the chosen scatter matches that found by Taylor et al. (2011) from the Galaxy and Mass Assembly survey. We show a summary of these model parameters and our priors in Table 2.

For each halo model, we sample from our posterior probability distribution,

$$\text{Post}(\theta|(\sigma, \delta\sigma, R), \text{Model}) \propto \frac{\mathcal{L}(\sigma|R, \text{Model}, \theta)}{\text{Prior}(\theta)}, \quad (17)$$

by using the affine-invariant ensemble MCMC algorithm of Goodman & Weare (2010). We run chains of 128 walkers for 4000 iterations, rejecting the first 2000 iterations where the MCMC might not have converged. We visually inspect the trace plots to verify that this is an adequate number of burn-in iterations.

4. Results

Table 2 summarizes the posterior distributions for the different halo mass models. The full posterior distributions are shown as marginalized 1D and 2D histograms in the Appendix.

We find that all models we consider are able to reproduce the observed velocity dispersion profile, as shown in Figure 2. We assess the relative quality of these models using leave-one-out cross validation (LOO-CV; Vehtari et al. 2015; Piironen & Vehtari 2017), finding no significant differences in the goodness-of-fit of FDM models relative to the CDM models. Translating the differences between models in their calculated LOO-CV information criteria into probabilities, we find that no model is more than ∼0.3 times as likely as any other model to best describe the data. In other words, the increase in goodness-

Table 2
Model Parameters for the Two CDM Halo Models from Paper I and the Two FDM Halo Models Presented in This Work

Parameter	Unit	Prior	CDM + NFW	FDM + NFW	CDM + $\alpha\beta\gamma$	FDM + $\alpha\beta\gamma$
$\log_{10}M_{200c}$	$M_\odot$	$\mathcal{U}(7, 15)$	$10.62^{+0.42}_{-0.30}$	$10.64^{+0.41}_{-0.32}$	$11.20^{+0.63}_{-0.63}$	$11.16^{+0.58}_{-0.58}$
$\log_{10}c_{200c}$	⋯	HMCR	$1.00^{+0.19}_{-0.20}$	$0.98^{+0.18}_{-0.19}$	$0.98^{+0.13}_{-0.16}$	$0.99^{+0.12}_{-0.14}$
$\log_{10}\Upsilon_*$	$M_\odot/L_{\odot,V}$	$\mathcal{N}(0.176, 0.1)$	$0.18^{+0.10}_{-0.10}$	$0.18^{+0.10}_{-0.10}$	$0.19^{+0.10}_{-0.10}$	$0.18^{+0.10}_{-0.10}$
$\tilde{\beta}_{\rm ani}$	⋯	$\mathcal{U}(-1.5, 1.5)$	$-0.24^{+0.10}_{-0.12}$	$-0.44^{+0.22}_{-0.29}$	$-0.05^{+0.08}_{-0.11}$	$-0.16^{+0.15}_{-0.39}$
$\log_{10}m_{22}$	10^{-22} eV	$\mathcal{U}(-3, 3)$	⋯	$0.34^{+0.76}_{-0.25}$	⋯	$0.51^{+0.62}_{-0.44}$
$\log_{10}r_{\rm sol}$	kpc	$\mathcal{U}(-2, 1)$	⋯	$-0.22^{+0.25}_{-0.34}$	⋯	$-0.16^{+0.25}_{-0.26}$

Note. The parameters are, from top to bottom, the halo virial mass, the halo concentration, the stellar mass-to-light ratio, the symmetrized anisotropy parameter ($\tilde{\beta}_{\rm ani} = -\log_{10}(1 - \beta_{\rm ani})$), the scalar field mass, and the soliton core radius. Columns show the chosen parameterization, relevant units, the prior distribution, and posterior summaries for the four halo models. For the priors, $\mathcal{U}(\ell, u)$ denotes a uniform prior with lower bound $\ell$and upper bound u, $\mathcal{N}(\mu, \sigma)$ denotes a Gaussian prior with mean μ and standard deviation σ, and HMCR refers to the halo mass–concentration relation prior (see Section 3.1). Posterior distributions are summarized as the median of the distribution and the distance to the 16th and 84th percentiles.

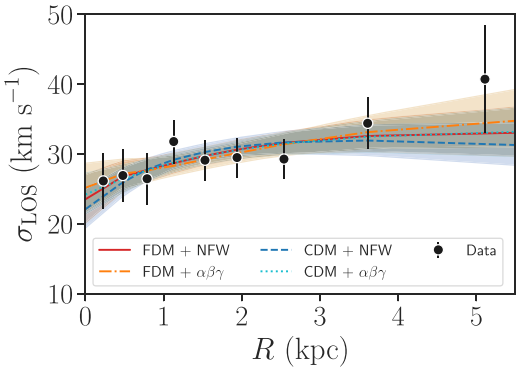

Figure 2. Posterior predictive checks on the velocity dispersion profiles for the FDM halo models compared with the kinematic observations, with the CDM halo models from Paper I shown for comparison. The red solid and orange dotted–dashed lines show the FDM halo models for the NFW and $\alpha\beta\gamma$ outer profiles. The dark blue dashed and cyan dotted lines show the CDM halo models for the NFW and $\alpha\beta\gamma$ profiles. The shaded regions cover the 16th through 84th percentiles of the distribution. We see that all four models do an adequate job of recovering the general trend of the kinematic data.

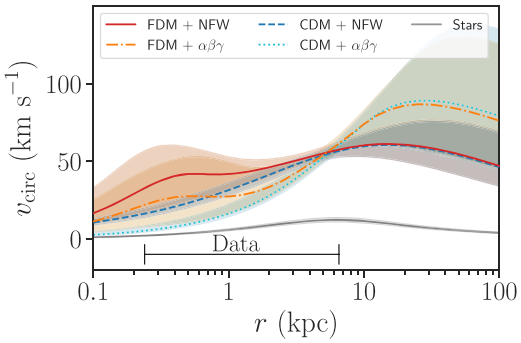

Figure 3. Circular velocity corresponding to the dynamical mass (DM + stars) for the FDM halo models, compared with their CDM halo counterparts. Note that these are profiles in de-projected (3D) radius, in contrast to the projected (2D) radial profiles shown in Figure 2. The bottom gray solid line shows the circular velocity profile corresponding to just the stellar mass for the NFW model. The black bar at the bottom indicates the spatial extent of the kinematic data. The dynamical mass within 5 kpc ($\sim R_e$) is well constrained by the data, but the mass within 1 kpc is degenerate with the chosen model.

of-fit from the FDM models is not enough to compensate for the increased model freedom (i.e., the additional model parameters).

As demonstrated in Figure 3, the dynamical mass profile is best constrained at the maximum radius of the kinematic tracers ($\sim$5 kpc), with $M_{\rm dyn}(<5\ {\rm kpc}) = 3.4^{+0.5}_{-0.4}(\pm 0.1) \times 10^9\ M_\odot$, where the systematic uncertainty (in parentheses) comes from the standard deviation between the four models.

Figure 3 also demonstrates the systematic effect that the choice of halo model has on the inferred circular velocity profile, with both CDM and FDM $\alpha\beta\gamma$ profiles preferring more massive halos than their associated NFW models by $\sim$0.5 dex. This is to be expected, as the cored $\alpha\beta\gamma$ models put less mass in the inner region (where we have kinematic constraints) compared to NFW models of the same halo mass. The differences in inferred halo mass between halo models are consistent within the statistical uncertainties from the spread in the posterior distributions, and the deviations indicates the difficulty in robustly extrapolating halo masses out to spatial scales where we lack data.

The analysis of higher order LOS velocity moments (e.g., kurtosis) may help in distinguishing cuspy density profiles (NFW) from shallower cored profiles ($\alpha\beta\gamma$), as discussed by Paper I. The high value of $h_4 = 0.13 \pm 0.05$ measured for the Dragonfly 44 stellar kinematic data slightly favors the $\alpha\beta\gamma$ model (predicted $h_4 = 0.01 \pm 0.01$) over the NFW model (predicted $h_4 = 0.03 \pm 0.02$). However, as h_4 is more susceptible to systematic biases than the velocity dispersion, we remain largely agnostic about which halo model (and hence which associated value for the halo mass) is correct.

As expected, the choice of CDM or FDM models has the most impact on the inner mass profile, with FDM models allowing a $\sim 10^9\ M_\odot$ core within 1 kpc. The inner mass distribution is degenerate with both the chosen model and the orbital anisotropy (see Figure 4), with the FDM models preferring more DM inside of 1 kpc and slightly more tangentially biased orbits. The primary modeling systematic affecting the anisotropy distribution, however, is the outer DM profile (NFW or $\alpha\beta\gamma$), with the NFW model preferring tangential orbits $\beta_{\rm ani} \sim -0.8$ and the $\alpha\beta\gamma$ model preferring isotropic orbits. We note that models with tangentially biased orbits will hide the signal of the $v_{\rm circ}$ soliton bump when projecting to the LOS velocity dispersion.

Figure 5 shows the ratio of the enclosed (i.e., cumulative) DM mass to stellar mass as a function of radius, and it confirms that Dragonfly 44 is DM-dominated ($M_{\rm DM}/M_* > 1$) independently of the considered cosmology (FDM/CDM) or degree of baryonic impacts (NFW/$\alpha\beta\gamma$), down to the smallest spatial scales probed by the data. As such, our inference on the mass-to-light ratio, Υ_*, is consistent with our chosen prior. With our

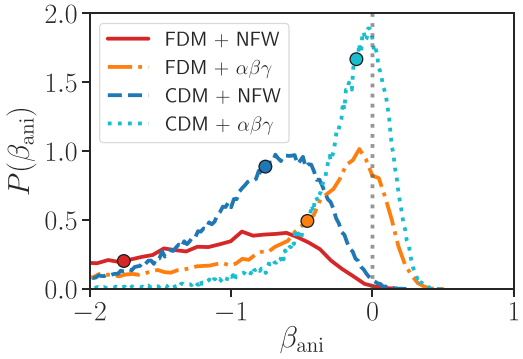

Figure 4. Posterior distributions of the orbital anisotropy parameter for the FDM halo models, compared with their CDM halo counterparts. The median of each distribution is marked by circles. The NFW models (both for CDM and FDM) prefer tangentially biased orbits ($\beta_{\rm ani} < 0$), with the tail of the distributions extending to the prior bound at $\tilde{\beta}_{\rm ani} = -1.5$ ($\beta_{\rm ani} = -30.6$). The $\alpha\beta\gamma$ models are consistent with isotropic orbits ($\beta_{\rm ani} = 0$, shown by the gray dotted line), but all of the posterior distributions are skewed in the direction of tangential anisotropy.

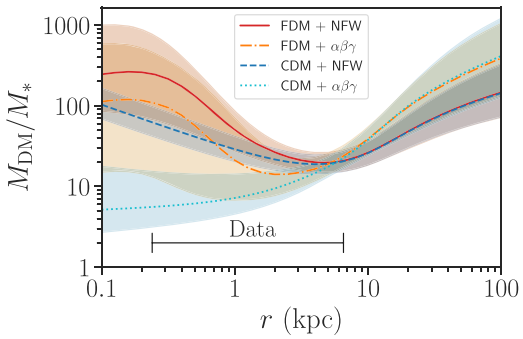

Figure 5. Ratio of DM to stellar mass as a function of radius for the FDM halo models, compared with their CDM halo counterparts. The black bar at the bottom indicates the spatial extent of the kinematic data. All four models show Dragonfly 44 to be DM-dominated ($M_{\rm DM}/M_* > 1$) down to ∼0.1 kpc.

chosen prior of $\log \Upsilon_* \sim 0.176 \pm 0.1$, $M_{\rm DM}/M_* \sim 20$ at $r = 5$ kpc, independently of the chosen mass model.

Looking at just the two FDM models, we see that they are consistent in their posterior soliton parameter distributions. Figure 6 shows the covariance between the scalar field mass, the total mass within the soliton core, and the ratio of the transition radius to the soliton scale radius. The modes of the distributions for both NFW and $\alpha\beta\gamma$ models have a $\sim 10^9\,M_\odot$ soliton core with a size of ∼0.6 kpc. We find a less likely second peak in the posterior distribution for the NFW model, toward a more massive scalar field ($m_{22} \sim 10$). This region has a soliton core with mass of $\sim 10^7\,M_\odot$ that rapidly transitions to the outer NFW halo profile. Thus, this second peak corresponds to models for which the DM scalar field is too massive to create a dynamically significant core on spatial scales probed by our data. For the $\alpha\beta\gamma$ model, this region of parameter space has a similar posterior density, but this manifests as a long tail toward higher scalar field masses rather than as a discrete second mode.

While the observable velocity dispersion of the FDM models will approach that of the CDM models in the limit as $m_{22} \to \infty$ (see the bottom right panel of Figure 1), we caution that this does *not* mean that the bounded m_{22} posterior distribution favors FDM over CDM. Rather, as discussed in the beginning of this section, we need to statistically account for the additional model freedom that the introduction of the soliton parameters provide.

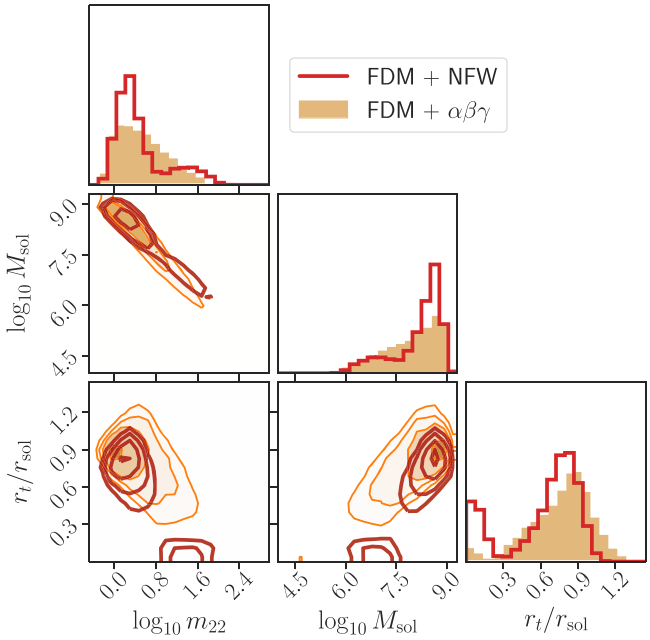

Figure 6. Posterior distributions for the scalar field mass in 10^{-22} eV, the mass within the soliton core (in $M_\odot$), and the ratio of the transition radius to the soliton core radius for the NFW (red, unfilled histograms) and $\alpha\beta\gamma$ (orange filled histograms) halo models. The FDM constraints are broadly similar between the two halo models, with both models favoring a core of mass $\sim 10^9\,M_\odot$. Both models show a mode in m_{22} of ∼2, with a broad posterior tail toward higher m_{22} values. For the NFW model, we see a second mode at high m_{22}, corresponding to a negligible core mass and hence a near-zero transition radius.

5. Discussion

We now focus on the question of whether or not the stellar dynamics of Dragonfly 44 are consistent with the FDM hypothesis and other constraints on FDM. We find qualitatively similar FDM constraints for both the NFW and $\alpha\beta\gamma$ models (see Figure 6), and so for the sake of simplicity we focus on the FDM + $\alpha\beta\gamma$ model.

5.1. Scalar Field Mass

We find the DM scalar field mass to be $m_{22} = 3.3^{+10.3}_{-2.1}$.

Figure 7 shows this range in the context of other observational constraints on the scalar field mass. The values we find for m_{22} are similar to those for the Local Group dSph galaxies from the study of Chen et al. (2017), who found $m_{22} \sim 1.8$. González-Morales et al. (2017) found a similar value ($m_{22} \sim 2.4$) from Jeans modeling of the same data, but they cautioned that the orbital anisotropy degeneracy could cause the scalar field mass inference to be biased high. Instead of using this Jeans analysis, they advocated instead for using mass estimators with multiple stellar subpopulations (e.g., Walker & Peñarrubia 2011), for which they derived an upper bound of $m_{22} < 0.4$.

Recent work by multiple authors (e.g., Armengaud et al. 2017; Iršič et al. 2017; Kobayashi et al. 2017; Nori et al. 2019) have used the Lyα forest power spectrum to test FDM. Less massive FDM particles would result in stronger deviations from ΛCDM at small spatial scales; thus these studies infer lower bounds on the scalar field mass, with m_{22} values ranging from 7 to 30.

There are a large number of modeling assumptions that go into this lower bound, ranging from the temperature evolution

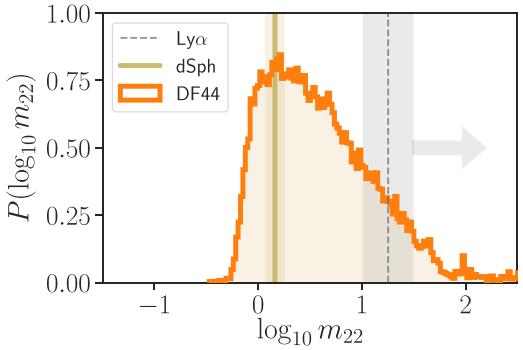

Figure 7. Posterior distributions of m_{22} from Dragonfly 44 (orange histogram) compared with constraints from the literature. A lower bound of $m_{22} \gtrsim 20$ from modeling of the Lyα forest (see sources in text) is shown by the gray dashed line, with the gray shaded region showing the range of lower bounds found in the literature. The constraint from dSph galaxies (Chen et al. 2017) is shown by the yellow solid line. We see that both inferences on m_{22} from Dragonfly 44 are consistent with the dSph constraints, but they are in tension with the Lyα constraint. Only ~10% of samples lie to the right of the Lyα lower bound.

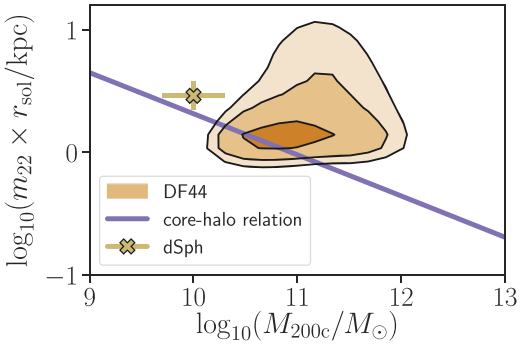

Figure 8. Posterior distribution of M_{200c} and $m_{22} \times r_{\rm sol}$ for Dragonfly 44 compared to the expected scaling relation. The violet line shows the functional relationship between halo mass and core size predicted by Schive et al. (2014a). The yellow × shows the inferred core size from dSph galaxies (Chen et al. 2017). There is a broad range of allowed core sizes, but the mode of the distribution is consistent with the expected scaling relation.

of the intergalactic medium during reionization (e.g., Garzilli et al. 2017) to different priors on cosmological parameters. In addition, Desjacques et al. (2018) found that even a relatively small self-interaction term in FDM can lead to instabilities that result in notable differences (with respect to CDM) in the cosmic web, complicating the interpretation of Lyα forest clustering. Due to degeneracies between reionization history and the growth of structure, it remains uncertain to what degree the FDM constraints from low-z galaxy dynamics and the high-z Lyα power spectrum are in tension with one another. Ultimately, FDM models that reproduce both galaxy dynamics and the observed Lyα forest power spectrum may need to go beyond the simple model considered here (e.g., Leong et al. 2019).

5.2. Core Size

The core sizes of soliton halos are predicted to scale with halo mass and scalar field mass as $r_{\rm sol} \propto m_{22}^{-1} M_h^{-1/3}$. We can see this by considering the following relations,

$$\begin{aligned} r_{\rm core} &\propto (mv)^{-1} \\ v &\propto \left(\frac{M_h}{r_h}\right)^{1/2} \\ r_h &\propto M_h^{1/3}, \end{aligned} \tag{18}$$

where the first one is from the de Broglie wavelength of the scalar field, the second relation comes from the virial theorem, and the third one comes from the definition of the halo virial radius. Indeed, inserting relevant constants, we can recover within order unity the scaling relation found from FDM simulations (Schive et al. 2014b):

$$\frac{r_{\rm sol}}{\rm kpc} = 5.304 \left(\frac{M_h}{10^9 M_\odot}\right)^{-1/3} m_{22}^{-1}. \tag{19}$$

We could in principle use Equation (19) as an informative prior on $r_{\rm sol}$, which would result in stronger constraints on m_{22}. However, because we let $r_{\rm sol}$ be a free parameter in our modeling of FDM halos, Equation (19) acts as an additional consistency test for the model. Figure 8 shows the posterior distribution of the core size (multiplied by the scalar field mass to remove its associated scaling) and the halo mass. The mode of the posterior is well-matched to this relation. In addition, we see that our derived core size for Dragonfly 44 is less than that derived by Chen et al. (2017) for their sample of lower halo mass dSph galaxies, consistent with the direction of the soliton core size–halo mass scaling relation.

5.3. Transition Radius

Another consistency check for our FDM models is the location of the transition from the inner soliton profile to the outer CDM-like profile (r_t from Equation (6)). For the outer $\alpha\beta\gamma$ profile, we infer $r_t = 0.5^{+0.4}_{-0.2}$ kpc and $r_t/r_{\rm sol} = 0.8^{+0.2}_{-0.3}$. As shown in Figure 6, these values are similar for the NFW model.

Using simulations of merging FDM halos, Mocz et al. (2017) interpreted this transition radius as the location where the energy density due to quantum pressure is equal to the classical kinetic energy density. They found this transition radius to occur at $r_t \sim 3.5 r_c$ (~1 $r_{\rm sol}$).

Recent work by Robles et al. (2019) identified a plausible range for this ratio of the transition radius to the soliton core radius. The maximum of this value is set by the requirement that the radius of the peak of the circular velocity profile is less than the virial radius. The corresponding minimum of this transition ratio is set by either the requirement of a local maximum in the circular velocity profile (for halos $\lesssim 10^{11} M_\odot$) or by the need for the peak of the velocity profile in the FDM halo to be less than that of the corresponding CDM halo (for more massive halos). For a halo of mass $\sim 10^{11} M_\odot$, these requirements translate to $0.6 \lesssim r_t/r_{\rm sol} \lesssim 1.2$.

These bounds, as well as the posterior distribution for this transition ratio, $r_t/r_{\rm sol}$, are shown in Figure 9. We recall that our definition of the soliton core radius differs from that used by Robles et al. (2019), requiring a conversion factor of 3.315. In addition, we show the same ratio as found in the simulations of Mocz et al. (2017). Most of the posterior mass (~70%) as well as the mode of the distribution is inside of these bounds, indicating that the inferred soliton transition radius is in agreement with the constraints for a reasonable FDM halo.

5.4. Future Work

One potentially rewarding area for future work would be testing FDM against galaxies with even higher halo masses

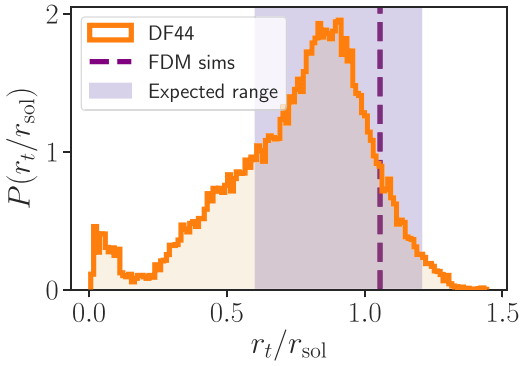

Figure 9. Posterior distribution of the ratio of the transition radius to the soliton scale radius for Dragonfly 44 (orange histogram), compared with the relevant bounds (violet region) for reasonable FDM halos at the inferred halo mass (see Robles et al. 2019, Section 2.2). The dotted violet line shows the approximate value from the FDM simulations of Mocz et al. (2017). Over two-thirds of the posterior mass for Dragonfly 44 is within these bounds, indicating good agreement with FDM predictions.

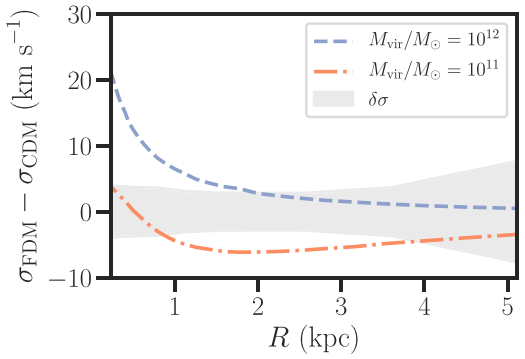

Figure 10. The difference in velocity dispersion between CDM and FDM models, as a function of radius. The orange dotted–dashed line corresponds to a $10^{11}\,M_\odot$ halo, similar to that inferred for Dragonfly 44. The blue dashed line corresponds to a $10^{12}\,M_\odot$ halo, and it demonstrates a much more detectable bump in the velocity dispersion inside of 1 kpc. The gray band indicates the observational uncertainties in velocity dispersion for the Dragonfly 44 data. Note that this uncertainty region does not take into account the systematic uncertainty in the halo mass profile from the unknown virial mass and concentration.

than that of Dragonfly 44. Figure 10 shows that the difference in velocity dispersion between a CDM halo model and an FDM model (both assuming an outer $\alpha\beta\gamma$ profile) is on the order of the observational uncertainties for a halo mass similar to that of Dragonfly 44. A $10^{12}\,M_\odot$ FDM halo would be much more readily detected with the current observational error budget. The field UDG DGSAT I, with its high velocity dispersion of $\sigma = 56$ km s^{-1} (Martín-Navarro et al. 2019), may be one such promising candidate.

As discussed in Paper I, modeling higher order LOSVD moments may help break the mass–anisotropy degeneracy. Another possibility would be to use the extensive globular star cluster system of some UDGs (van Dokkum et al. 2017) as tracers of the potential. Such multi-population Jeans modeling can also mitigate the uncertainties from orbital anisotropy (e.g., Oldham & Auger 2016; Zhu et al. 2016; Wasserman et al. 2018).

Most simulation studies of FDM in the literature have not modeled the impact of baryons on the density structure of DM halos (with Bar et al. 2019 being a notable exception). Our crude method for marginalizing over this uncertainty was to try models with the best fit DM profiles from the hydrodynamical simulations of Di Cintio et al. (2014), which naturally assumed a CDM cosmology. Stellar feedback may be critical in forming UDGs (Di Cintio et al. 2017a; Chan et al. 2018; Jiang et al. 2019) and would likely affect the properties of soliton cores in FDM. Galaxy formation studies with warm dark matter and self-interation dark matter (e.g., Di Cintio et al. 2017b; Fitts et al. 2019; Despali et al. 2019) have helped identify better ways of discriminating between available models, and we believe dedicated studies of galaxy formation in a FDM cosmology will be necessary to disentangle the effects of baryonic feedback and new DM physics on the observable DM mass distribution.

6. Conclusions

We applied equilibrium dynamical models to new spatially resolved spectroscopy of the integrated starlight of the UDG Dragonfly 44. We considered FDM halo models in which DM consists of an ultralight scalar field.

While we were unable to statistically distinguish between our proposed halo mass models, we were able to test the consistency of the FDM halo models. If we assume an FDM cosmology, the inferred scalar field mass and soliton core size are consistent with a range of FDM predictions, including the core size–halo mass scaling relation and the radius of transition between the soliton core and the outer halo.

The inferred scalar field mass from the Dragonfly 44 data is largely in agreement with other constraints from galaxy dynamics, however it is in tension with results from modeling the Lyα forest power spectrum. Possible solutions to these disagreements include accounting for any self-interactions in the scalar field or allowing for a mixture of FDM and CDM. Future work is needed to fully quantify this tension and to determine if FDM is a viable alternative to CDM.

We gratefully acknowledge the support of the National Science Foundation via grants AST-1312376, AST-1518294, AST-1613582, AST-1616598, and AST-1616710, as well as *HST* grant *HST*-GO-14643.

A.J.R. was supported as a Research Corporation for Science Advancement Cottrell Scholar. D.A.F. thanks the ARC for funding via DP160101608. A.V. is supported by an NSF Graduate Research Fellowship. This work was supported by a NASA Keck PI Data Award, administered by the NASA Exoplanet Science Institute. Data presented herein were obtained at the W. M. Keck Observatory from telescope time allocated to the National Aeronautics and Space Administration through the agency's scientific partnership with the California Institute of Technology and the University of California. The Observatory was made possible by the generous financial support of the W. M. Keck Foundation. The authors wish to recognize and acknowledge the very significant cultural role and reverence that the summit of Maunakea has always had within the indigenous Hawaiian community. We are most fortunate to have the opportunity to conduct observations from this mountain.

Facilities: Keck:II (KCWI), *HST*.

Software: NumPy (Walt et al. 2011), matplotlib (Hunter 2007), astropy (Astropy Collaboration et al. 2018), Julia (Bezanson et al. 2017), DifferntialEquations.jl (Rackauckas & Nie 2017).

Appendix
Posterior Distributions

In Figure 11 show the 1D and 2D marginalized posterior distributions for each of the four halo models. The parameterization and associated units are shown in Table 2.

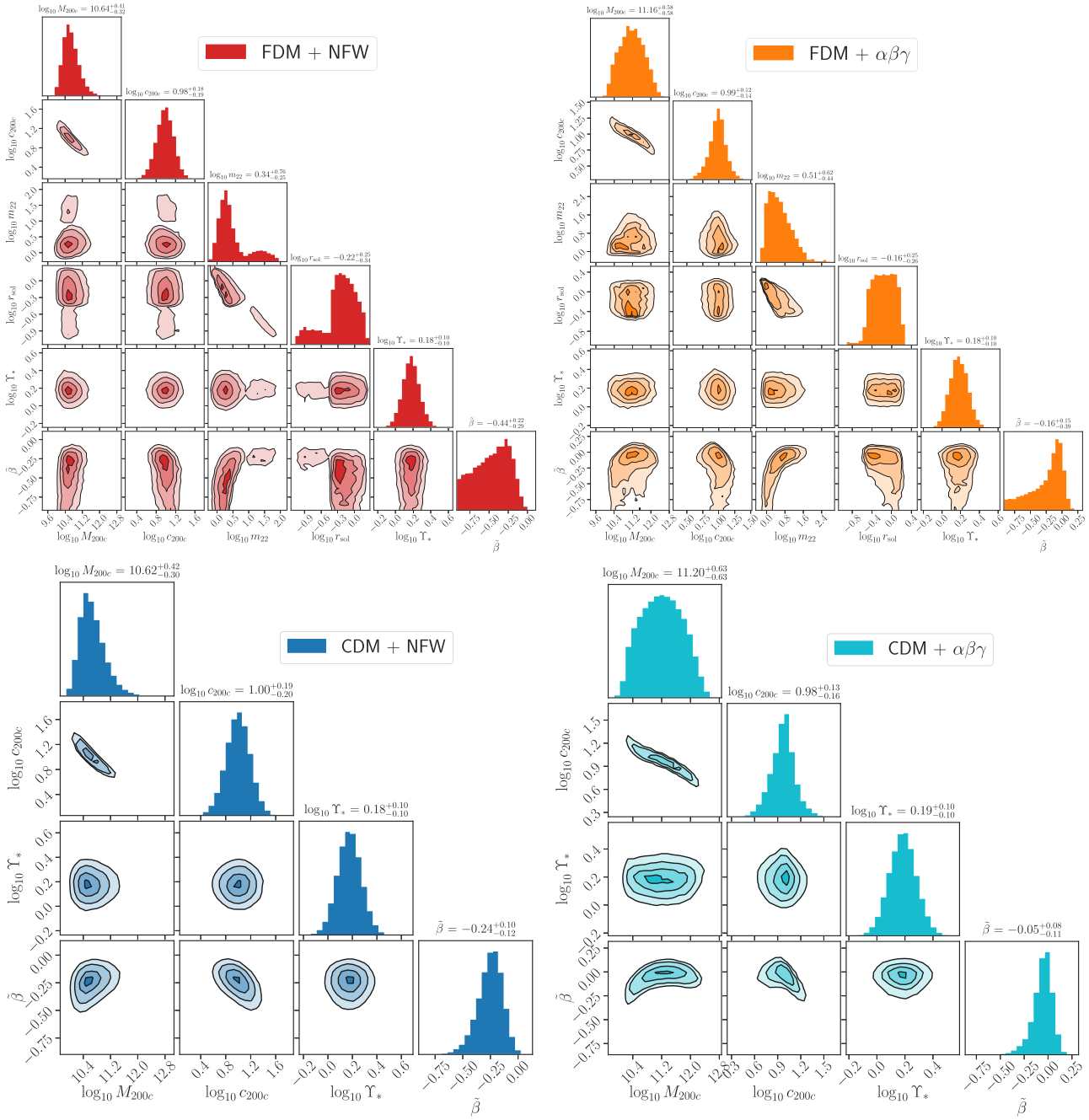

Figure 11. Marginalized posterior distributions for the four halo models. The top panels show the FDM models from this work. The bottom panels show the CDM models from Paper I. Left panels are for NFW halo profiles, and right panels show the results for the $\alpha\beta\gamma$ halo profiles. Within both top (FDM) panels the parameters are (from left to right, or top to bottom) the log of the halo mass, the log of the halo concentration, the log scalar field mass, the log soliton scale radius, the log of the stellar mass-to-light ratio, and the symmetric parameterization of the anisotropy parameter. Contours show isodensity surfaces from 0.5 to 2.0 "sigma" levels (for a 2D Gaussian).

ORCID iDs

Asher Wasserman https://orcid.org/0000-0003-4235-3595
Aaron J. Romanowsky https://orcid.org/0000-0003-2473-0369
Jean Brodie https://orcid.org/0000-0002-9658-8763
Shany Danieli https://orcid.org/0000-0002-1841-2252
Roberto Abraham https://orcid.org/0000-0002-4542-921X
Alexa Villaume https://orcid.org/0000-0003-1887-0621

References

Akerib, D. S., Alsum, S., Araújo, H. M., et al. 2017, PhRvL, 118, 021303
Aprile, E., Aalbers, J., Agostini, F., et al. 2018, PhRvL, 121, 111302
Armengaud, E., Palanque-Delabrouille, N., Yèche, C., Marsh, D. J. E., & Baur, J. 2017, MNRAS, 471, 4606
Astropy Collaboration, Price-Whelan, A. M., Sipőcz, B. M., et al. 2018, AJ, 156, 123
Bar, N., Blas, D., Blum, K., & Sibiryakov, S. 2018, PhRvD, 98, 083027
Bar, N., Blum, K., Eby, J., & Sato, R. 2019, PhRvD, 99, 103020
Bernal, T., Fernández-Hernández, L. M., Matos, T., & Rodríguez-Meza, M. A. 2018, MNRAS, 475, 1447
Bertone, G., Hooper, D., & Silk, J. 2005, PhR, 405, 279
Bezanson, J., Edelman, A., Karpinski, S., & Shah, V. 2017, SIAMR, 59, 65
Bozek, B., Fitts, A., Boylan-Kolchin, M., et al. 2019, MNRAS, 483, 4086
Bozek, B., Marsh, D. J. E., Silk, J., & Wyse, R. F. G. 2015, MNRAS, 450, 209
Bringmann, T., & Hofmann, S. 2007, JCAP, 2007, 016
Buckley, M. R., & Peter, A. H. G. 2018, PhR, 761, 1
Bullock, J. S., & Boylan-Kolchin, M. 2017, ARA&A, 55, 343
Calabrese, E., & Spergel, D. N. 2016, MNRAS, 460, 4397
Carlson, E. D., Machacek, M. E., & Hall, L. J. 1992, ApJ, 398, 43
Chan, T. K., Kereš, D., Wetzel, A., et al. 2018, MNRAS, 478, 906
Chen, S.-R., Schive, H.-Y., & Chiueh, T. 2017, MNRAS, 468, 1338
Colpi, M., Shapiro, S. L., & Wasserman, I. 1986, PhRvL, 57, 2485
Davis, M., Lecar, M., Pryor, C., & Witten, E. 1981, ApJ, 250, 423
Desjacques, V., Kehagias, A., & Riotto, A. 2018, PhRvD, 97, 023529
Despali, G., Sparre, M., Vegetti, S., et al. 2019, MNRAS, 484, 4563
Di Cintio, A., Brook, C. B., Dutton, A. A., et al. 2014, MNRAS, 441, 2986
Di Cintio, A., Brook, C. B., Dutton, A. A., et al. 2017a, MNRAS, 466, L1
Di Cintio, A., Tremmel, M., Governato, F., et al. 2017b, MNRAS, 469, 2845
Diemer, B., & Kravtsov, A. V. 2015, ApJ, 799, 108
Dine, M., Fischler, W., & Srednicki, M. 1981, PhLB, 104, 199
El-Zant, A. A., Freundlich, J., & Combes, F. 2016, MNRAS, 461, 1745
Fitts, A., Boylan-Kolchin, M., Bozek, B., et al. 2019, MNRAS, 490, 962
Garzilli, A., Boyarsky, A., & Ruchayskiy, O. 2017, PhLB, 773, 258
González-Morales, A. X., Marsh, D. J. E., Peñarrubia, J., & Ureña-López, L. A. 2017, MNRAS, 472, 1346
Goodman, J., & Weare, J. 2010, Comm. App. Math. and Comp. Sci., 5, 65
Hayashi, K., & Obata, I. 2019, arXiv:1902.03054
Hernquist, L. 1990, ApJ, 356, 359
Hlozek, R., Grin, D., Marsh, D. J. E., & Ferreira, P. G. 2015, PhRvD, 91, 103512
Hu, W., Barkana, R., & Gruzinov, A. 2000, PhRvL, 85, 1158
Hui, L., Ostriker, J. P., Tremaine, S., & Witten, E. 2017, PhRvD, 95, 043541
Hunter, J. D. 2007, CSE, 9, 90
Iršič, V., Viel, M., Haehnelt, M. G., Bolton, J. S., & Becker, G. D. 2017, PhRvL, 119, 031302
Jiang, F., Dekel, A., Freundlich, J., et al. 2019, MNRAS, 487, 5272
Kobayashi, T., Murgia, R., De Simone, A., Iršič, V., & Viel, M. 2017, PhRvD, 96, 123514
Koda, J., Yagi, M., Yamanoi, H., & Komiyama, Y. 2015, ApJL, 807, L2
Lee, J.-W., & Koh, I.-G. 1996, PhRvD, 53, 2236
Leong, K.-H., Schive, H.-Y., Zhang, U.-H., & Chiueh, T. 2019, MNRAS, 484, 4273
Lora, V., & Magaña, J. 2014, JCAP, 9, 011
Lovell, M. R., Gonzalez-Perez, V., Bose, S., et al. 2017, MNRAS, 468, 2836
Mamon, G. A., & Łokas, E. L. 2005, MNRAS, 363, 705
Marrodán Undagoitia, T., & Rauch, L. 2016, JPhG, 43, 013001
Marsh, D. J. 2016, PhR, 643, 1
Marsh, D. J. E., & Niemeyer, J. C. 2019, PhRvL, 123, 051103
Marsh, D. J. E., & Pop, A.-R. 2015, MNRAS, 451, 2479
Martín-Navarro, I., Romanowsky, A. J., Brodie, J. P., et al. 2019, MNRAS, 484, 3425
Martizzi, D., Teyssier, R., & Moore, B. 2013, MNRAS, 432, 1947
Matos, T., Vázquez-González, A., & Magaña, J. 2009, MNRAS, 393, 1359
Mihos, J. C., Durrell, P. R., Ferrarese, L., et al. 2015, ApJL, 809, L21
Mocz, P., Vogelsberger, M., Robles, V. H., et al. 2017, MNRAS, 471, 4559
Nadler, E. O., Gluscevic, V., Boddy, K. K., & Wechsler, R. H. 2019, ApJ, 878, L32
Navarro, J. F., Frenk, C. S., & White, S. D. M. 1997, ApJ, 490, 493
Nori, M., Murgia, R., Iršič, V., Baldi, M., & Viel, M. 2019, MNRAS, 482, 3227
Oldham, L. J., & Auger, M. W. 2016, MNRAS, 457, 421
Peccei, R. D., & Quinn, H. R. 1977, PhRvL, 38, 1440
Piironen, J., & Vehtari, A. 2017, Statistics and Computing, 27, 711
Planck Collaboration, Aghanim, N., Akrami, Y., et al. 2018, arXiv:1807.06209
Pontzen, A., & Governato, F. 2012, MNRAS, 421, 3464
Profumo, S. 2017, An Introduction to Particle Dark Matter (Singapore: World Scientific)
Rackauckas, C., & Nie, Q. 2017, JORS, 5, 15
Robles, V. H., Bullock, J. S., & Boylan-Kolchin, M. 2019, MNRAS, 483, 289
Rocha, M., Peter, A. H. G., Bullock, J. S., et al. 2013, MNRAS, 430, 81
Schaller, M., Frenk, C. S., Bower, R. G., et al. 2015, MNRAS, 451, 1247
Schive, H.-Y., Chiueh, T., & Broadhurst, T. 2014a, NatPh, 10, 496
Schive, H.-Y., Chiueh, T., Broadhurst, T., & Huang, K.-W. 2016, ApJ, 818, 89
Schive, H.-Y., Liao, M.-H., Woo, T.-P., et al. 2014b, PhRvL, 113, 261302
Taylor, E. N., Hopkins, A. M., Baldry, I. K., et al. 2011, MNRAS, 418, 1587
Tegmark, M., Eisenstein, D. J., Strauss, M. A., et al. 2006, PhRvD, 74, 123507
van Dokkum, P., Abraham, R., Brodie, J., et al. 2016, ApJL, 828, L6
van Dokkum, P., Abraham, R., Romanowsky, A. J., et al. 2017, ApJL, 844, L11
van Dokkum, P., Wasserman, A., Danieli, S., et al. 2019, ApJ, 880, 91
van Dokkum, P. G., Abraham, R., Merritt, A., et al. 2015, ApJL, 798, L45
Vehtari, A., Gelman, A., & Gabry, J. 2015, arXiv:1507.04544
Viel, M., Lesgourgues, J., Haehnelt, M. G., Matarrese, S., & Riotto, A. 2005, PhRvD, 71, 063534
Walker, M. G., & Peñarrubia, J. 2011, ApJ, 742, 20
Walt, S. v. d., Colbert, S. C., & Varoquaux, G. 2011, CSE, 13, 22
Wasserman, A., Romanowsky, A. J., Brodie, J., et al. 2018, ApJ, 863, 130
Weinberg, D. H., Bullock, J. S., Governato, F., Kuzio de Naray, R., & Peter, A. H. G. 2015, PNAS, 112, 12249
Wittman, D., Golovich, N., & Dawson, W. A. 2018, ApJ, 869, 104
Zhu, L., Romanowsky, A. J., van de Ven, G., et al. 2016, MNRAS, 462, 4001